# Photoacoustic Microscopy of Peritubular Capillary Function and Oxygen Metabolism in Mouse Kidney

Naidi Sun<sup>1,5,†</sup>, Shuqiu Zheng<sup>2,4,†</sup>, Diane L. Rosin<sup>3,4</sup>, Nabin Poudel<sup>2,4</sup>, Junlan Yao<sup>2,4</sup>, Heather Perry<sup>2,4</sup>, Rui Cao<sup>1</sup>, Mark D. Okusa<sup>2,4,\*</sup>, and Song Hu<sup>1,5,\*</sup>

<sup>1</sup>Department of Biomedical Engineering, University of Virginia, Charlottesville, VA 22908, United States

<sup>2</sup>Department of Medicine, Division of Nephrology, University of Virginia, Charlottesville, VA 22908, United States

<sup>3</sup>Department of Pharmacology, University of Virginia, Charlottesville, VA 22908, United States

<sup>4</sup>Center for Immunity, Inflammation and Regenerative Medicine, University of Virginia,

Charlottesville, VA 22908, United States

<sup>5</sup>Current address: Department of Biomedical Engineering, Washington University in St. Louis, St. Louis, MO 63130, United States

Mark D. Okusa, Division of Nephrology and Center for Immunity, Inflammation and Regenerative Medicine, University of Virginia Health System, Charlottesville, VA 22908, United States, Email: mdo7y@virginia.edu, Phone: 434-924-2187

Song Hu, Department of Biomedical Engineering, Washington University in St. Louis, St. Louis, MO 63130, United States, Email: <a href="mailto:songhu@wustl.edu">songhu@wustl.edu</a>, Phone: 314-935-3637

## **Running Headline**

PAM of peritubular capillary function & metabolism

<sup>†</sup>Equal contributions

<sup>\*</sup>Correspondence:

#### Abstract

Microcirculatory changes and oxidative stress have long been associated with acute kidney injury (AKI). Despite substantial progress made by two-photon microscopy of microvascular responses to AKI in rodent models, little is known about the underlying changes in blood oxygen delivery and tissue oxygen metabolism. To fill this gap, we have developed a label-free kidney imaging technique based on photoacoustic microscopy (PAM), which enables simultaneous quantification of hemoglobin concentration (C<sub>Hb</sub>), oxygen saturation of hemoglobin (sO<sub>2</sub>), and blood flow in peritubular capillaries *in vivo*. Based on these microvascular parameters, microregional oxygen metabolism is quantified for the first time. We demonstrated the utility of this technique by studying renal hemodynamic and oxygen-metabolic responses to AKI in mice subject to lipopolysaccharide-induced sepsis. Dynamic PAM of the peritubular capillary function and tissue oxygen metabolism revealed that sepsis induced an acute and significant reduction in peritubular capillary sO<sub>2</sub>, which was concomitant with a marked reduction in kidney ATP levels and contrasted with the minimal changes in peritubular capillary flow and plasma creatinine. This technique opens new opportunities to study microvascular and metabolic dysfunction in acute and chronic kidney diseases.

## **Keywords**

Photoacoustic microscopy, acute kidney injury, sepsis, peritubular capillary function, oxygen metabolism

#### Introduction

Sepsis-associated acute kidney injury (S-AKI) is a common cause of AKI, accounting for nearly 50% of AKI cases in the intensive care unit, and is associated with high morbidity and mortality. Despite subtle changes in histology, a complex set of host responses to infection is responsible for organ dysfunction including AKI. Sepsis is associated with adaptive and maladaptive responses that lead to endothelial dysfunction, inflammation, and disturbances in coagulation and cellular metabolism. These responses lead to important macrocirculatory and microcirculatory changes, which have been revealed by magnetic resonance imaging (MRI), ultrasound, high-resolution microcomputed tomography (micro-CT), and two-photon microscopy (TPM) in both animal models and human patients.

As a direct consequence of the microcirculatory changes in sepsis, tissue hypoxia leads to kidney dysfunction and injury. Understanding the mechanism of tissue hypoxia in S-AKI requires direct assessment of microvascular oxygen delivery and tissue oxygen metabolism, which, however, remains an unmet challenge. Existing imaging techniques are inadequate to address this challenge due to the following limitations: 1) the mesoscopic resolution of MRI and acoustic-resolution photoacoustic imaging is insufficient to resolve the micro-regional metabolic dysfunction due to microcirculatory changes;<sup>9</sup> 2) ultrasound and micro-CT cannot measure blood oxygenation; 3) the long lifetime of phosphorescent probes required by TPM to measure blood oxygenation limits its imaging speed and hampers dynamic monitoring.

To address this challenge, we have developed a photoacoustic microscopy (PAM)-based technique for intravital imaging of the mouse kidney in a label-free manner. The renal PAM enables simultaneous imaging of hemoglobin concentration (C<sub>Hb</sub>), oxygen saturation of hemoglobin (sO<sub>2</sub>), and blood flow at the peritubular capillary level, based on which microregional metabolic rate of oxygen (MRO<sub>2</sub>) is derived for the first time. We have demonstrated the utility of this technique by studying the acute hemodynamic and oxygen-metabolic responses of the mouse kidney to lipopolysaccharide (LPS)-induced S-AKI.

## Methods

All methodologies are detailed in the Supplementary File.

#### **Results**

Intravital PAM of mouse kidney

PAM (Supplementary Figure S1) enables simultaneous imaging of peritubular capillary C<sub>Hb</sub>, sO<sub>2</sub>, and blood flow in the mouse kidney, showing heterogeneous distributions of blood perfusion and oxygenation across the capillary network (Figure 1a), which echoes Hirakawa *et al.*'s observations using intravital phosphorescence lifetime imaging.<sup>10</sup> The PAM-resolved peritubular capillary structure (2-D projection is shown in Figure 1b, and 3-D reconstitution is shown in Figure 1c and Supplementary Video 1) is also consistent with previous TPM findings<sup>8</sup> and is beyond the reach of mesoscopic photoacoustic imaging.<sup>9</sup>

In addition to the multifaceted peritubular capillary function, PAM also provides depthresolved information based on the time-of-flight ultrasonic detection. As shown in Figure 1d, the upper and lower boundaries of the PAM signals in a representative cross-sectional scan (indicated by the yellow dashed lines) can be readily identified, from which the penetration of PAM is estimated to be ~200 µm—comparable to that of TPM in the rodent kidney.<sup>8</sup> Instead of projecting the maximum amplitude of the depth-resolved signal across the entire range, as shown in Figure 1a, dividing the 200-µm range into multiple sections with a 20-µm thickness results in a series of depth-specific images and cross-sectional profiles of the insets, showing the depth-sectioning capability of PAM (Figure 1e).

Hemodynamic responses of kidney under normoxia vs. hypoxia

Before applying the intravital PAM to AKI studies, we tested its utility for kidney blood oxygenation and flow imaging in an established model of experimental hypoxia. In comparison to the multi-parametric PAM images acquired in the mouse kidney under normoxia (Figure 2a), inhalation of the gas mixture with only 14% oxygen (Figure 2b) led to a significant decrease in sO<sub>2</sub> and increase in flow speed, but no change in C<sub>Hb</sub> (Figure 2c). The PAM-based measurements under both normoxia and hypoxia are in good agreement with those previously obtained with the use of direct oximetry. <sup>11,12</sup>

Acute hemodynamic and oxygen-metabolic responses of kidney to S-AKI

Using PAM, we monitored the hemodynamic and oxygen-metabolic responses of the mouse kidney to S-AKI over an 80-min period following the administration of LPS (Figure 3) and compared it with a saline-treated control group (Supplementary Figure S2), based on which quantitative analyses were performed to compare the differential responses between the two groups (Figure 4).

Throughout the monitoring period, there was no significant change in C<sub>Hb</sub> in response to LPS injection (Figures 3a and 4a). In contrast, sO<sub>2</sub> started to decline 10 min after the injection and showed a ~30% decrease persisted from 20–80 min (Figures 3b and 4b). Accompanying the significant and enduring decrease in blood oxygenation was an abrupt increase in peritubular capillary flow (~10%) within 10 min of LPS injection, which, however, quickly rebounded and remained at the baseline level after 20 min (Figures 3c and 4c). Combining the C<sub>Hb</sub>, sO<sub>2</sub>, and blood flow measurements enabled the quantification of micro-regional MRO<sub>2</sub>, which showed a biphasic response to the LPS injection—gradually increasing and peaking at 60 min after injection (130% of the pre-injection value) and then decreasing afterwards (Figures 3d and 4d). As expected, the control group did not respond to saline injection (Supplementary Figure S2 and Figure 4).

Further, we analyzed the heterogeneities of blood oxygenation and flow by plotting the distributions of sO<sub>2</sub> and flow speed in pixel-based histograms (Supplementary Figures S3 and S4, respectively). Our results show that, besides overall changes in the average values across the entire imaging area, changes in the histogram distributions are also considerable, indicating heterogenenous changes in blood oxygenation and flow during S-AKI. It is worth noting that the imaging areas in different animals were carefully selected to be within the same cortical region (Supplementary Figures S1c). Due to the limited penetration depth of PAM, our results only represent the heterogeneity in the kidney cortex.

## Biochemical changes in S-AKI

Hematoxylin and eosin (H&E) staining and periodic acid-Schiff staining (PAS) were performed to detect the histopathological differences in renal tissues between the saline- and

LPS-injected animals. In contrast to the normal morphology in the saline group (Figure 5a, left), sloughing of tubular cells and apoptosis of nephrons were observed in the LPS group (Figure 5a, right). Furthermore, the renal function was assessed. Although no difference in the plasma creatinine concentration was observed in the first 80 min following LPS or saline injection (Figure 5b), there was a significant reduction in kidney ATP levels in this early stage of LPS-induced sepsis (Figure 5c).

The time course of ATP response—starting to decrease within the first 10 min and reaching a nadir at 40 min—closely resembled that of  $sO_2$  shown in Figure 4b. The strong correlation between the LPS-induced dynamic changes in  $sO_2$  and ATP ( $r^2 = 0.92$  as shown in Supplementary Figure S5a), which was much more significant than that in the saline-injected control group ( $r^2 = 0.23$  as shown in Supplementary Figure S5b), suggested a link between tissue hypoxia and mitochondrial metabolic dysfunction in the early phase of S-AKI.

#### **Discussion**

The pathophysiology of S-AKI involves microcirculatory changes.<sup>4</sup> Intravital microscopy has revealed striking heterogeneity of microcirculatory flow patterns in sepsis, <sup>13</sup> but the underlying oxygen-metabolic changes remain poorly understood due to technical limitations. <sup>14</sup> We have filled this gap by developing a PAM-based intravital kidney imaging platform, which enables simultaneous, label-free imaging of C<sub>Hb</sub>, sO<sub>2</sub>, and blood flow at the peritubular capillary level in the mouse kidney with a penetration depth comparable to TPM (~200 μm).

Exploiting the high resolution and new oxygen-metabolic insights offered by this technique, we observed increased heterogeneity of the microvascular blood oxygenation and flow, as well as micro-regional oxygen metabolism, in the early phase of S-AKI (Supplementary Figure S6b–d), which echoes and extends the previous observation in microvascular flow<sup>13</sup>. Moreover, we observed that blood oxygenation in the kidney microvasculature decreased significantly following the onset of sepsis and showed a strong temporal correlation with the change in kidney ATP levels (Supplementary Figure S5a). Proximal tubules depend primarily on oxidative phosphorylation to generate ATP, and both oxidative phosphorylation and ATP generation are impaired during sepsis. The progressively decreased kidney microvascular sO<sub>2</sub> might underlie the impaired ATP production in sepsis. Since there was very little change in peritubular capillary

blood flow, the significant reduction in blood oxygenation suggests an enhanced oxygen extraction and increased MRO<sub>2</sub> of the kidney tissue after the onset of S-AKI, which echoes previous observations in patients with sepsis-induced cardiac dysfunction<sup>16</sup> and postcardiac surgery patients with AKI<sup>17</sup>. The increased oxygen consumption and reduced ATP production might reflect the uncoupling of electron transport from ATP production in mitochondria and could be associated with increased production of ROS,<sup>18</sup> which has been observed in diabetic hyperglycemia<sup>19</sup> and intracerebral hemorrhage<sup>20</sup>. In accordance with this hypothesis, TPM has observed altered energy metabolism and accelerated generation of ROS in LPS-treated mice.<sup>21</sup> Nevertheless, it is also possible that the changes in oxygen extraction and metabolism might be due to the interaction of endotoxin with TLR4 receptors on tubule segments, which alters cellular metabolism. In support of this concept, TPM has shown that bacterial endotoxin is filtered and internalized by proximal tubules.<sup>22</sup> Thus, future research is warranted to reveal the molecular mechanisms underlying the increased oxygen consumption and reduced ATP production in S-AKI, which might be a promising therapeutic target.

In summary, we have developed a PAM-based intravital imaging technique for dynamic and multifaceted monitoring of microvascular function and oxygen metabolism in the mouse kidney cortex, which opens new opportunities for mechanistic studies of microcirculatory and metabolic dysfunction in kidney diseases. Future developments by shifting the photoacoustic excitation to the near-infrared spectral region<sup>23</sup> and implementing localization-based super-resolution imaging<sup>24</sup> hold the potential to extend the penetration of PAM into the medulla of the rodent kidney.

#### **Disclosures**

All the authors declared no competing interests.

#### References

- 1. Angus DC, van der Poll T. Severe sepsis and septic shock. *N Engl J Med*. 2013;369:840-851.
- 2. Bellomo R, Kellum JA, Ronco C. Acute kidney injury. *The Lancet*. 2012;380:756-766.
- 3. Hotchkiss RS, Monneret G, Payen D. Sepsis-induced immunosuppression: from cellular dysfunctions to immunotherapy. *Nat Rev Immunol*. 2013;13:862-874.
- 4. Zarbock A, Gomez H, Kellum JA. Sepsis-induced acute kidney injury revisited: pathophysiology, prevention and future therapies. *Curr Opin Crit Care*. 2014;20:588-595.
- 5. Kobayashi H, Kawamoto S, Jo S-K, et al. Renal tubular damage detected by dynamic micro-MRI with a dendrimer-based magnetic resonance contrast agent. *Kidney Int*. 2002;61:1980-1985.
- 6. Lindner Jonathan R., Song Ji, Christiansen Jonathan, Klibanov Alexander L., Xu Fang, Ley Klaus. Ultrasound assessment of inflammation and renal tissue injury with microbubbles targeted to P-selectin. *Circulation*. 2001;104:2107-2112.
- 7. Ehling J, Bábíčková J, Gremse F, et al. Quantitative micro-computed tomography imaging of vascular dysfunction in progressive kidney diseases. *J Am Soc Nephrol*. 2016;27:520-532.
- 8. Dunn KW, Sandoval RM, Kelly KJ, et al. Functional studies of the kidney of living animals using multicolor two-photon microscopy. *Am J Physiol Cell Physiol.* 2002;283:C905-916.
- 9. Ogunlade O, Connell JJ, Huang JL, et al. In vivo three-dimensional photoacoustic imaging of the renal vasculature in preclinical rodent models. *Am J Physiol Renal Physiol*. 2018;314:F1145-F1153.
- 10. Hirakawa Y, Mizukami K, Yoshihara T, et al. Intravital phosphorescence lifetime imaging of the renal cortex accurately measures renal hypoxia. *Kidney Int.* 2018;93:1483-1489.
- 11. Abdelkader A, Ho J, Ow CPC, et al. Renal oxygenation in acute renal ischemia-reperfusion injury. *Am J Physiol-Renal*. 2014;306:F1026-F1038.
- 12. Galat JA, Robinson AV, Rhodes RS. Effect of hypoxia on renal flow. *J Trauma*. 1988;28:955-961.
- 13. Koh IHJ, Menchaca-Diaz JL, Koh TH, et al. Microcirculatory evaluation in sepsis: a difficult task. *Shock*. 2010;34 Suppl 1:27-33.
- 14. Evans RG. Another step forward for methods for studying renal oxygenation. *Kidney Int.* 2019;96:552-554.

- 15. Parikh SM. Therapeutic targeting of the mitochondrial dysfunction in septic acute kidney injury. *Curr Opin Crit Care*. 2013;19:554-559.
- 16. Potz BA, Sellke FW, Abid MR. Endothelial ROS and impaired myocardial oxygen consumption in sepsis-induced cardiac dysfunction. *J Intensive Crit Care*. 2016;2:1-15.
- 17. Redfors B, Bragadottir G, Sellgren J, Swärd K, Ricksten S-E. Acute renal failure is NOT an "acute renal success"--a clinical study on the renal oxygen supply/demand relationship in acute kidney injury. *Crit Care Med.* 2010;38:1695-1701.
- 18. Salin K, Auer SK, Rey B, Selman C, Metcalfe NB. Variation in the link between oxygen consumption and ATP production, and its relevance for animal performance. *Proc R Soc B*. 2015;282:20151028.
- 19. Nishikawa T, Edelstein D, Du XL, et al. Normalizing mitochondrial superoxide production blocks three pathways of hyperglycaemic damage. *Nature*. 2000;404:787-790.
- 20. Sook Kim-Han Jeong, Kopp Sarah J., Dugan Laura L., Diringer Michael N. Perihematomal mitochondrial dysfunction after intracerebral hemorrhage. *Stroke*. 2006;37:2457-2462.
- 21. Hato T, Winfree S, Day R, et al. Two-photon intravital fluorescence lifetime imaging of the kidney reveals cell-type specific metabolic signatures. *J Am Soc Nephrol*. 2017;28:2420-2430.
- 22. Kalakeche R, Hato T, Rhodes G, et al. Endotoxin uptake by S1 proximal tubular segment causes oxidative stress in the downstream S2 segment. *J Am Soc Nephrol*. 2011;22:1505-1516.
- 23. Hai P, Yao J, Maslov KI, Zhou Y, Wang LV. Near-infrared optical-resolution photoacoustic microscopy. *Opt Lett.* 2014;39:5192-5195.
- 24. Kim J, Kim JY, Jeon S, Baik JW, Cho SH, Kim C. Super-resolution localization photoacoustic microscopy using intrinsic red blood cells as contrast absorbers. *Light Sci Appl.* 2019;8:103.

## Acknowledgments

This study was supported, in part, by the National Science Foundation CBET-2023988. The content is solely the responsibility of the authors and does not necessarily represent the official views of the funding agencies. The authors thank the UVA Research Histology Core for their assistance in preparation of histology slides.

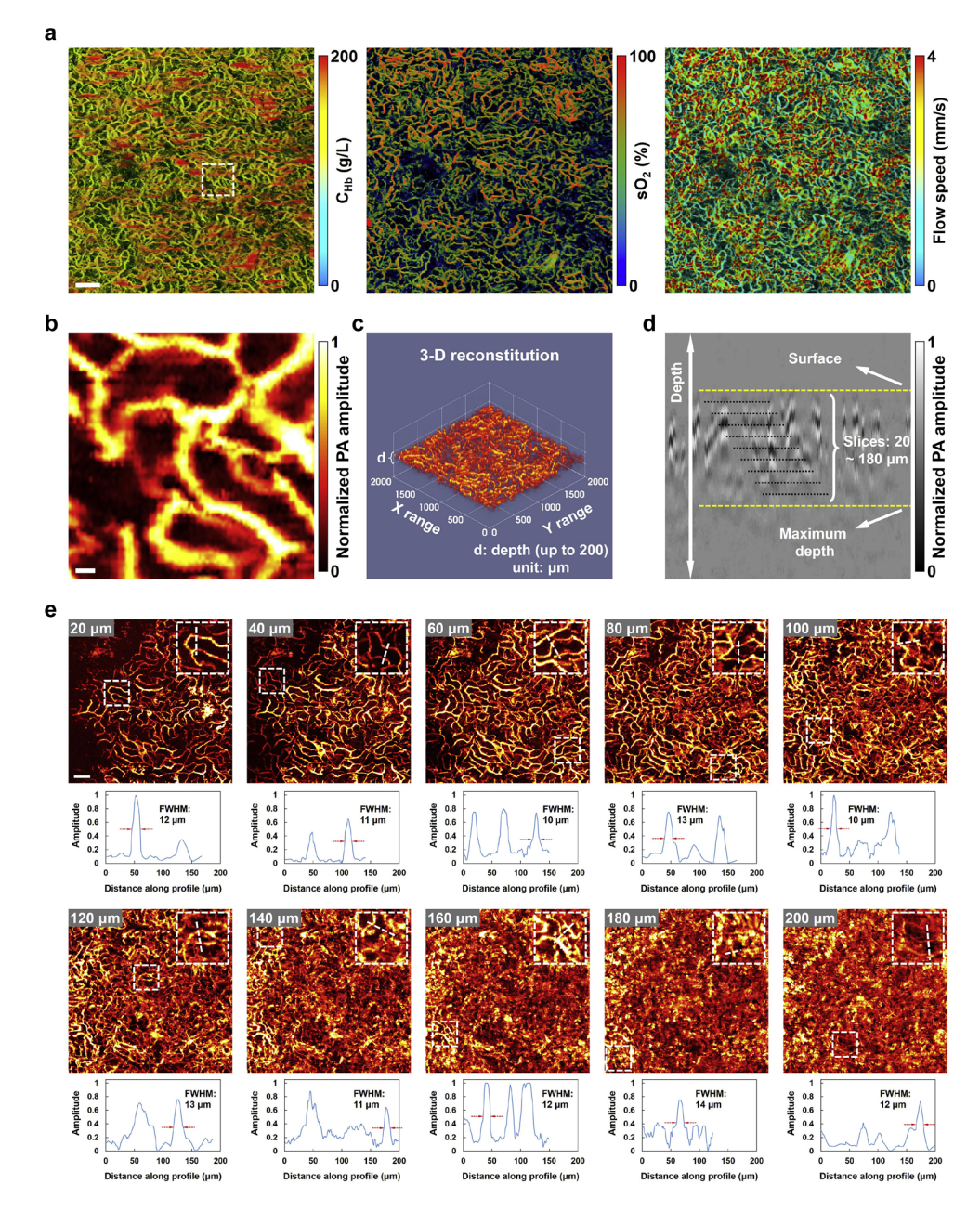


Figure 1. Intravital photoacoustic (PA) microscopy of the mouse kidney, showing microvascular function and depth-resolved microvascular structure. (a) Quantitative measurements of the total concentration of hemoglobin ( $C_{Hb}$ ), oxygen saturation of hemoglobin ( $sO_2$ ), and blood flow speed in the kidney microvasculature. Bar =  $200 \mu m$ . (b) Close-up view of the white boxed region in (a), showing the clearly resolved peritubular capillaries. Bar =  $20 \mu m$ . (c) Three-dimensional (3-D) reconstitution of the renal microvasculature. (d) A representative cross-sectional (i.e., B-scan) image, showing densely packed microvascular cross sections throughout the 200- $\mu m$  penetration depth. (e) A series of maximum-amplitude-projection images obtained at different depth ranges, from the surface to the maximum depth with a 20- $\mu m$  interval. Insets show the clearly resolved kidney capillaries, whose cross-sectional profiles show that their diameters are around  $10 \mu m$ . Bar =  $200 \mu m$ . FWHM, full width at half maximum.

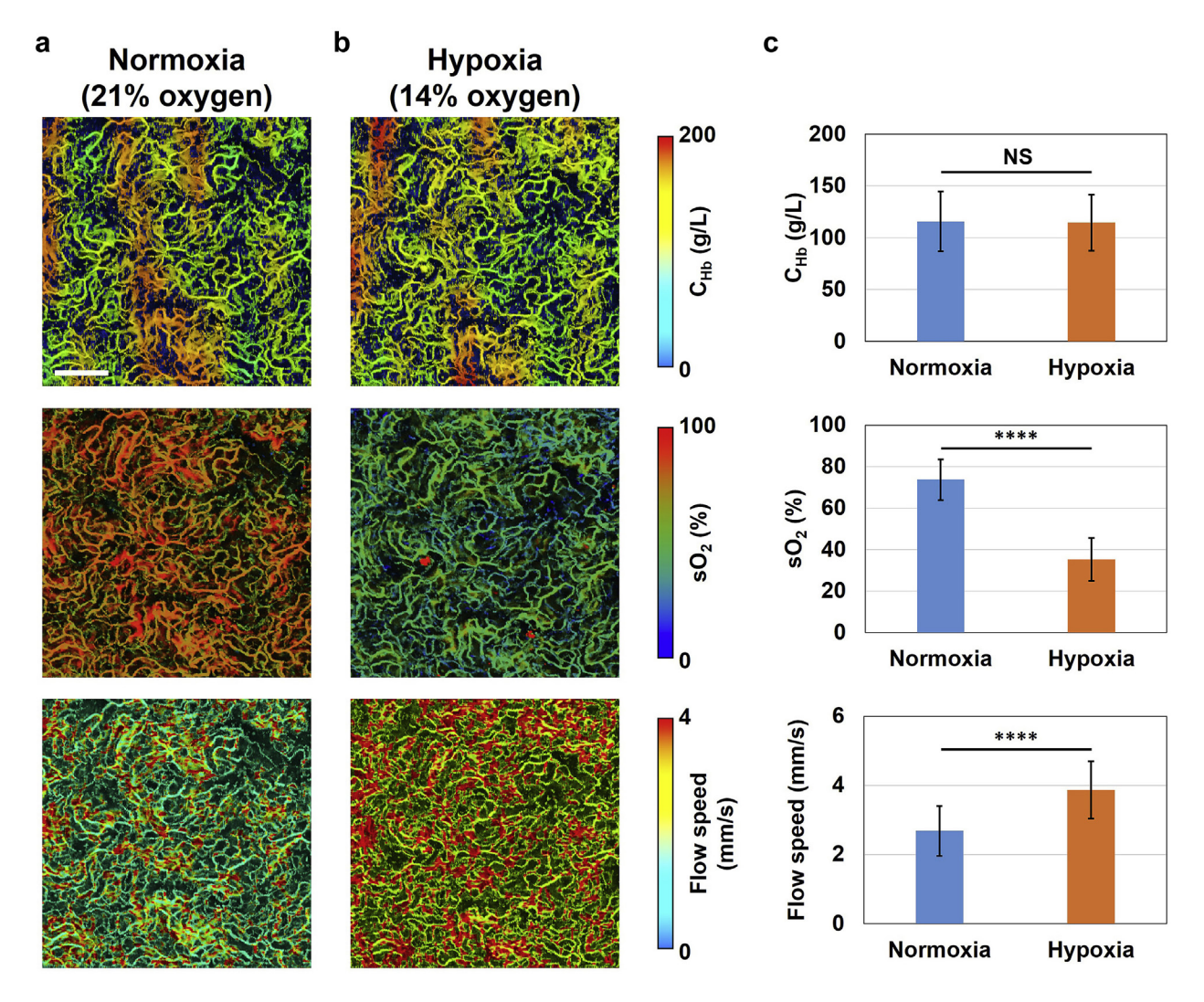


Figure 2. Intravital <u>photoacoustic microscopy</u> of total concentration of hemoglobin ( $C_{Hb}$ ), <u>oxygen saturation</u> of hemoglobin ( $sO_2$ ), and blood flow speed in the mouse **kidney.** Shown under (**a**) normoxia and (**b**) <u>hypoxia</u>. (**c**) Hypoxia-induced changes in the  $C_{Hb}$ ,  $sO_2$ , and blood flow speed, based on pixel-wise comparison. \*\*\*\*P < 0.0001. Data are mean  $\pm$  SEM. Bar = 200  $\mu$ m. NS, not significant.

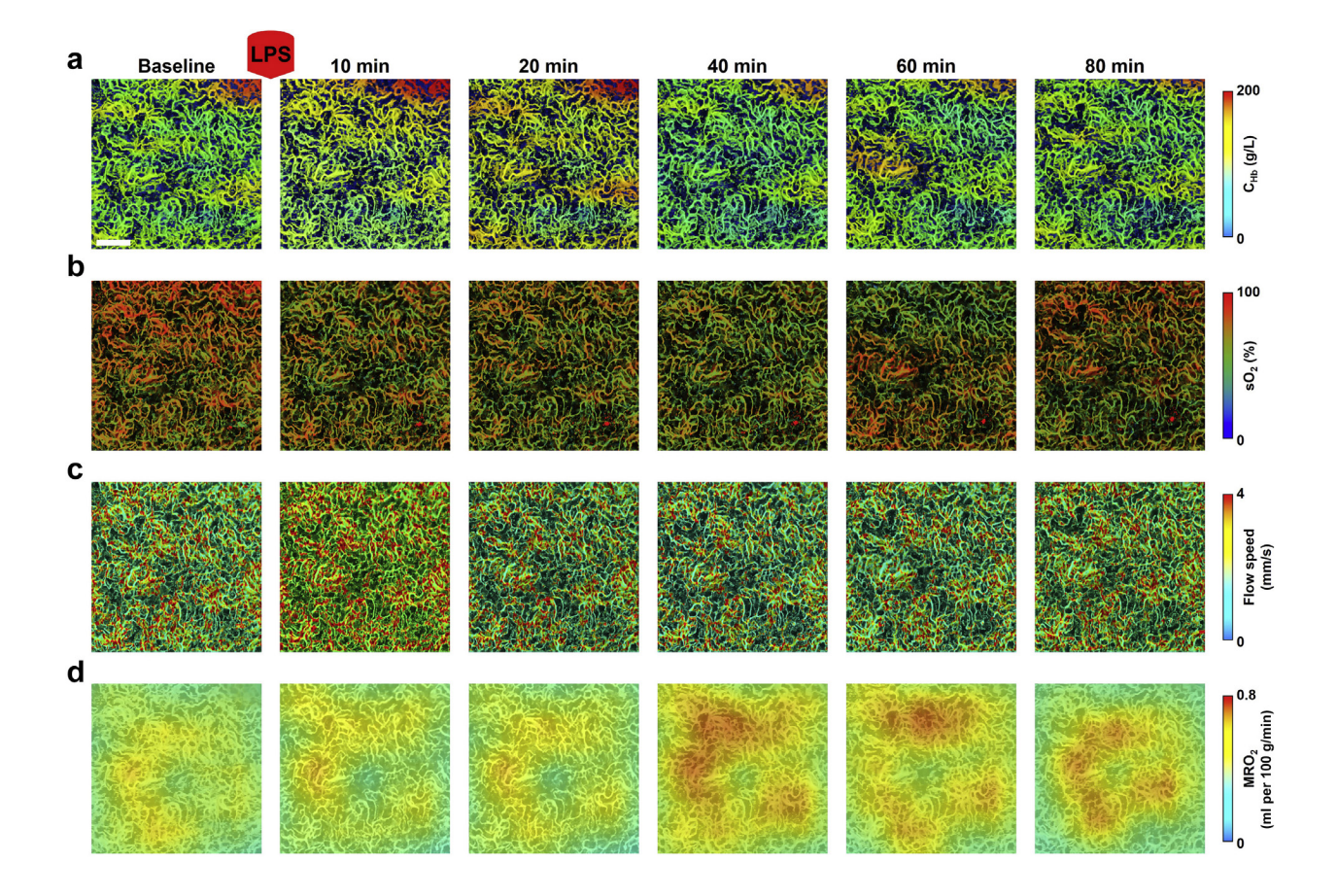


Figure 3. Time-lapse <u>photoacoustic microscopy</u> of renal microvascular and oxygen-metabolic responses to <u>lipopolysaccharide</u> (LPS)-induced <u>acute kidney injury</u>. (a) Total concentration of hemoglobin ( $C_{Hb}$ ), (b) <u>oxygen saturation</u> of hemoglobin ( $sO_2$ ), (c) blood flow speed, and (d) metabolic rate of oxygen (MRO<sub>2</sub>) images acquired before and 10 minutes, 20 minutes, 40 minutes, 60 minutes, and 80 minutes following LPS injection, respectively. Bar = 200  $\mu$ m. This experiment was repeated in 6 animals.

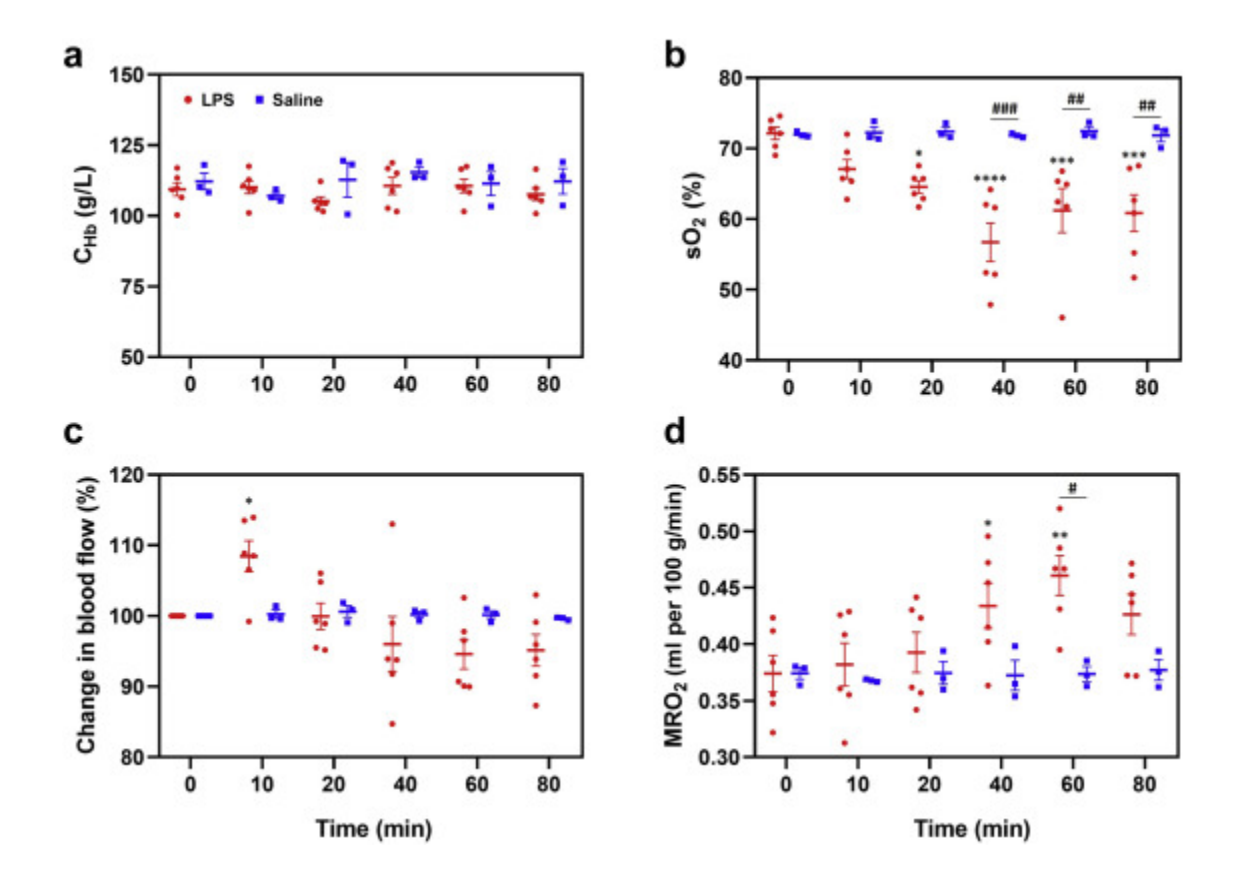


Figure 4. Comparison of the multifaceted microvascular and oxygen-metabolic responses to <u>lipopolysaccharide</u> (LPS) versus saline treatment. Comparison includes (a) total concentration of hemoglobin ( $C_{Hb}$ ), (b) <u>oxygen saturation</u> of hemoglobin ( $sO_2$ ), (c) blood flow speed, and (d) metabolic rate of oxygen (MRO<sub>2</sub>). \*P < 0.05, \*\*P < 0.01, \*\*\*P < 0.001, and \*\*\*\*P < 0.0001 indicate statistically significant differences from the corresponding baseline values acquired at 0 minutes (i.e., before treatment). #P < 0.05, ##P < 0.01, and ###P < 0.001 indicate statistically significant differences between the time-matched measurements in the LPS- (n = 6) and saline-treated (n = 3) groups. Data are mean ± SEM.

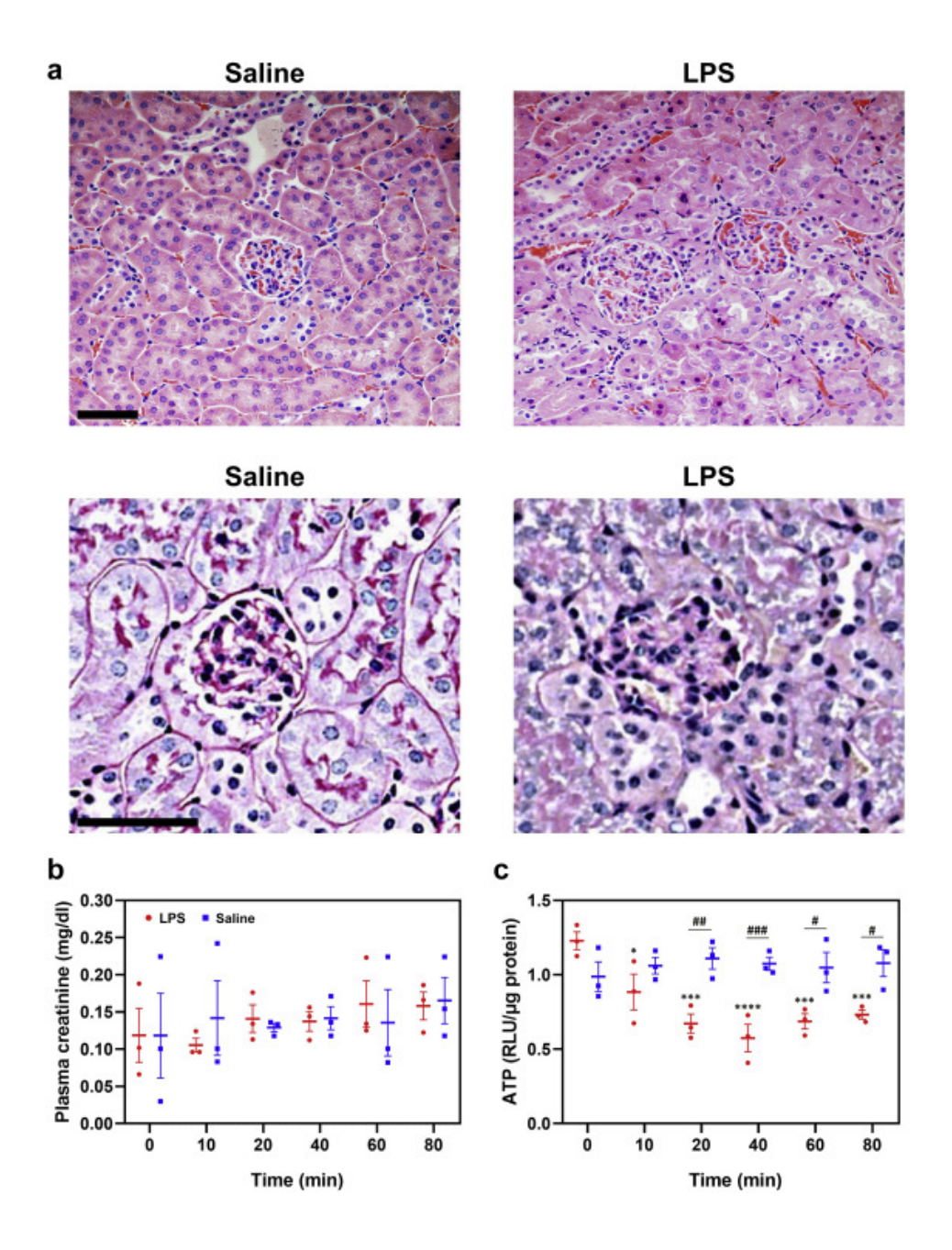


Figure 5. Differences in <u>histopathology</u> and plasma creatinine and kidney adenosine triphosphate (ATP) levels between the <u>lipopolysaccharide</u> (LPS)- and saline-treated groups. (a) Histopathology imaged with (upper) <u>hematoxylin</u> and <u>eosin</u> staining and (lower) periodic acid—Schiff staining. Graphs show (b) plasma creatinine and (c) kidney ATP levels between the LPS- and saline-treated groups. (a) Bars =  $100 \mu m$  (upper) and  $50 \mu m$  (lower). \*P < 0.05, \*\*\*P < 0.001, and \*\*\*\*P < 0.0001 indicate statistically significant differences from the corresponding baseline values acquired at 0 minutes (i.e., before treatment). #P < 0.05, ##P < 0.01, and ###P < 0.001 indicate statistically significant differences between the time-matched measurements in the LPS- and saline-treated groups (n = 3 per time points; n = 18 per group). Data are mean ± SEM. RLU, relative luminescence units.

## **Supplementary Methods**

#### Animals

C57BL/6 mice (male; 8-12 weeks old; Jackson Laboratory, Bar Harbor, ME) were used in this study. Mice were maintained under a controlled light-dark cycle (12:12-hour) with free access to food and water. Experiments were performed in accordance with the National Institutes of Health's guide for Care and Use of Laboratory Animals. All procedures were approved by the Institutional Animal Care and Use Committee at the University of Virginia.

#### LPS-induced S-AKI model

Mice in the S-AKI group were given a single intraperitoneal injection of LPS (5 mg/kg; *Escherichia coli* 0111:B4 strain, Sigma Aldrich, St. Louis, MO), and the control group received an equal volume of saline. Animals were randomly assigned to the saline- (control) and LPS-injected groups.

#### Normoxia vs. hypoxia.

For normoxia, the oxygen concentration in the inhalation gas was 21% (medical-grade air, AI M-T, Praxair, Danbury, CT). For hypoxia, the medical-grade air was mixed with nitrogen gas (medical-grade nitrogen, NI-H, Praxair, Danbury, CT) to achieve a reduced oxygen concentration of 14%, which was confirmed by a clinical anesthesia monitor (Capnomac Ultima, Datex-Ohmeda, Chicago, IL). To keep the animals under anesthesia during PAM imaging, 2% isoflurane was vaporized by the inhalation gas at a flow rate of 1.5 L/min.

# Working principles of PAM

Our PAM technique enables simultaneous quantification of multiple microvascular parameters, including the total concentration of hemoglobin (C<sub>Hb</sub>), oxygen saturation of hemoglobin (sO<sub>2</sub>), and blood flow *in vivo*. Briefly, by analyzing the statistical fluctuation of the PAM signal caused by the Brownian motion of erythrocytes, C<sub>Hb</sub> can be derived. With a dual-wavelength measurement at 532 and 558 nm, oxy- and deoxy-hemoglobin can be differentiated

based on spectroscopic analysis, from which sO<sub>2</sub> can be derived. By analyzing the flow-induced decorrelation of successively acquired signals, PAM can also quantify microvascular blood flow. S1 The detailed methodology for the statistical, spectroscopic, and correlation analyses of CHb, sO<sub>2</sub>, and blood flow has been reported by us before. S2

As shown in Supplementary Figure S1a, two nanosecond-pulsed lasers (wavelength: 532 nm; BX40-2-G, EdgeWave, Würselen, Germany) were used in the PAM system for mouse kidney imaging. The output powers of both lasers were regulated by neutral-density filters (NDF; NDC-50C-2M, Thorlabs, Newton, NJ). One of the laser beams was coupled into a polarizationmaintaining single-mode fiber (PM-SMF; F-SPA, Newport, Irvine, CA) via a fiber collimator (FC; CFC-11X-A, Thorlabs, Newton, NJ) for the Raman scattering-based wavelength conversion. S3 The output of the PM-SMF was collimated by another fiber collimator (FC; CFC-11X-A, Thorlabs, Newton, NJ) and purified by a bandpass filter (BPF; CT560/10bp, Chroma, Bellows Falls, VT) to isolate the 558-nm spectral component. Then, the 558-nm beam and the 532-nm beam from the other laser were combined via a dichroic beam splitter (DBS; FF552-Di02-25x36, Semrock, Rochester, NY), coupled into a single-mode fiber (SMF; P1-460B-FC-1, Thorlabs, Newton, NJ) through an objective lens (M-10X, Newport, Irvine, CA), and routed to the scanning head. To compensate for the intensity fluctuation of the laser, ~5% of the light was picked off by a beam sampler (BSA; BSF10-A, Thorlabs, Newton, NJ) and monitored by a highspeed photodiode (PD; FDS100, Thorlabs, Newton, NJ). In the scanning head (Supplementary Figure S1b), the output of the single-mode fiber was collimated by an achromatic doublet (DL; AC127-025-A, Thorlabs, Newton, NJ), and then focused by another identical doublet and a correction lens (CL; LA1207-A, Thorlabs, Newton, NJ). A customized, ring-shaped ultrasonic transducer (UT; inner diameter: 2.2 mm; outer diameter: 4.0 mm; focal length: 6.0 mm; center frequency: 35 MHz; 6-dB bandwidth: 70%) was used for convenient light excitation through the central opening with minimal interference with the ultrasonic detection. The transducer was submerged in a customized water tank for acoustic coupling. The entire scanning head was mounted on a 3-axis motorized stage for 2-D raster scan along the transverse directions and automated adjustment of the focal plane along the vertical direction. The lasers, motorized stage, photodiode, and data acquisition card (ATS9350, AlazarTech, Pointe-Claire, Canada) were controlled by a field-programmable gate array (PCIe-7841R, National Instruments, Austin, TX) through a self-developed LabVIEW program.

The experimental setting for intravital kidney imaging is illustrated in Supplementary Figure S1b, where the mouse kidney was surgically exteriorized, immobilized by agar, and held in position by a 3-D printed kidney cup and a metal rod. Throughout the imaging process (see details in "*Intravital PAM imaging*"), the mouse was anesthetized and placed on a heating plate (SRFG-303/10, Omega, Norwalk, CT) to keep its body temperature at 37 °C, and the cortical region highlighted by the white dashed box was imaged (Supplementary Figure S1c).

## Intravital PAM imaging

Mice were anesthetized with a mixture of ketamine hydrochloride (120 mg/kg) and xylazine hydrochloride (12 mg/kg),<sup>S4</sup> and additional anesthetic was supplemented as needed. Throughout the imaging experiment, the mice were maintained under general anesthesia and the body temperature was kept at 37 °C, which was monitored by a rectal probe. The left kidney was exposed by surgically opening the left flank. After gently teasing away tissue around the renal pedicle, the kidney was exteriorized and immobilized in the kidney cup filled with agar, which was designed to prevent possible stretching of the renal vessels. Transparent to both light and ultrasound, agar was used to prevent dehydration and to insulate the kidney from motion caused by respiration and heartbeat. After solidification of the agar solution (1% wt/vol; cooled to 40°C), a thin layer of ultrasound gel (~1 mm) was applied to the surface of the agar for acoustic coupling. The animal holder was then carefully raised to bring the gel in gentle contact with the bottom of the water tank, which was filled with temperature-maintained deionized water (37 °C).

For the normoxia vs. hypoxia experiment, PAM imaging was first performed under the normoxic condition (21% oxygen). Then, the animals were subject to systemic hypoxia by inhaling the oxygen-nitrogen mixed gas (14% oxygen). For the S-AKI experiment, LPS (5 mg/kg) was administered after the baseline imaging. Then, time-lapse PAM was performed at 10, 20, 30, 40, 50, 60 and 80 min after LPS injection. For a field of view of 1×1 mm², as shown in Figure 3 and Supplementary Figure S2, the acquisition time was ~10 min. At the end of the experiment, plasma was collected (see details in "*Plasma creatinine assay*"). The mice were euthanized by overdose of xylazine and ketamine, followed by kidney tissue collection. Additional animals were treated with LPS and euthanized at various time points to measure the plasma creatinine and kidney ATP levels.

Assessment of the spatial heterogeneity in microvascular hemodynamics and metabolism

To quantify the heterogenous distribution of microvascular hemodynamics and oxygen metabolism, an established image processing approach was applied. Strist, gray-level spatial dependence matrices were obtained from individual hemodynamic and metabolic images by applying a standard MATLAB function (*i.e.*, graycomatrix). Then, the homogeneity of each image was calculated from this matrix by applying another MATLAB function (*i.e.*, graycoprops). The calculated homogeneity spans from 0 to 1, which respectively correspond to minimal and maximum homogeneity (*i.e.*, maximum and minimal heterogeneity).

#### Plasma creatinine assay

Blood was collected from the retro-orbital sinus of the animal under anesthesia, and plasma was prepared by centrifuging heparinized blood at  $4,800 \times g$  for 5 min. Plasma creatinine was measured by enzymatic assay according to the manufacturer's protocol (Diazyme Laboratories, Poway, CA), with twice of the recommended sample volume. The accuracy of this method has been verified by liquid chromatography-mass spectrometry. S6,S7

## Kidney ATP assay

ATP levels in the mouse kidney were determined by CellTiter-Glo Luminescent Cell Viability Assay kit (G7571, Promega, Madison, WI). ATP extraction was performed using buffer saturated phenol (Invitrogen#15513039) as described previously (PMID# 22541816) with slight modifications. Briefly, the kidney tissue was placed in buffer saturated phenol, cut into small pieces and homogenized. 500  $\mu$ L of homogenate was transferred to an Eppendorf tube containing 100  $\mu$ L of chloroform and 100  $\mu$ L of water and centrifuged for 10 min at 10,000  $\times$ g, at 4 °C. The upper aqueous phase was collected for ATP analysis. 20  $\mu$ L of the aqeous phase was mixed with 20  $\mu$ L of CellTiter-Glo reagent and luminescence signal was measured immediately. Protein concentration was measured from the initial tissue homogenate using BCA assay and luminesce signal was normalized to the protein concentration of the homogenate. Protein concentration was measured by optical density with a spectrophotometer according to the absorbance at 260

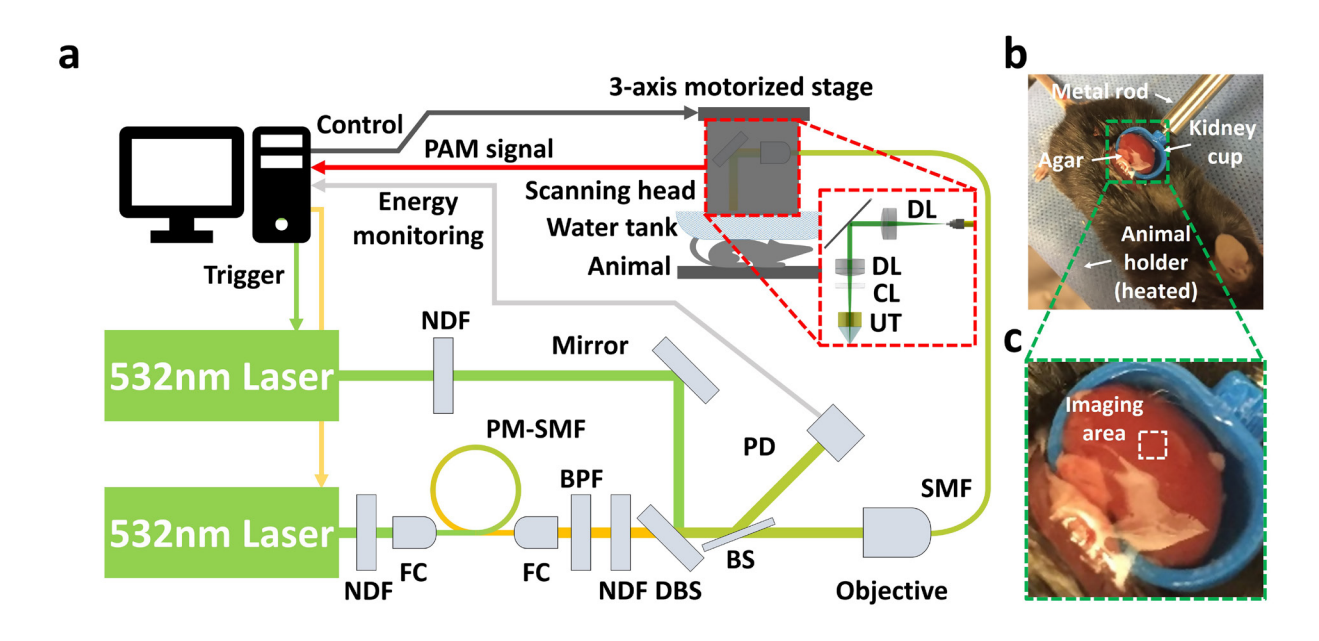
nm and the 260 nm/280 nm absorbance ratio (Nanodrop®, Thermo Scientific, Wilmington, DE). The luminescence signal is proportional to the amount of ATP.

Hematoxylin-eosin (H&E) staining and periodic acid-Schiff (PAS) staining

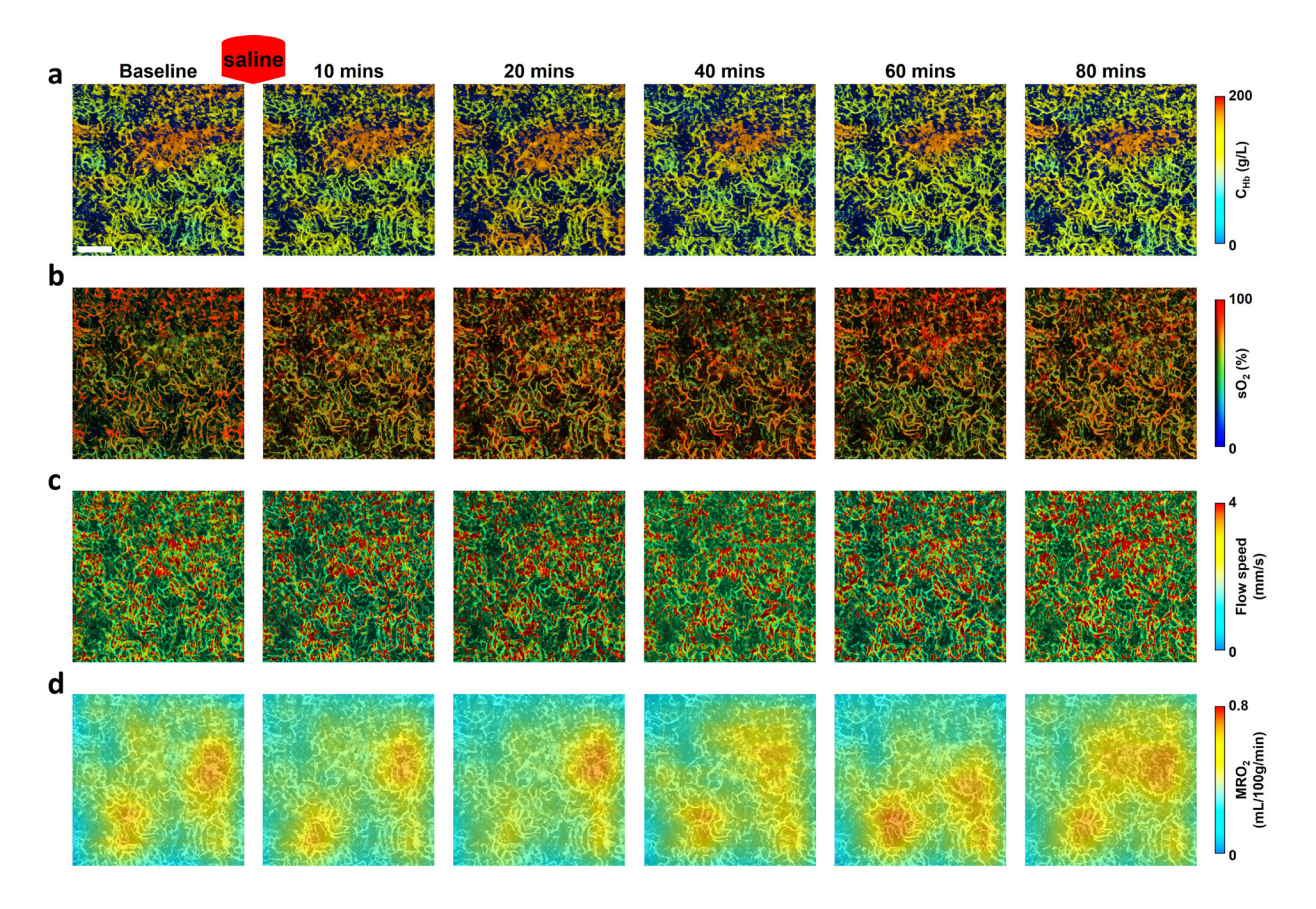
Mice were euthanized after 24 hours post injection, and kidney tissues from the right kidney were collected and fixed in 4% neutral formaldehyde solution for 24 hours at 40 °C. Paraffin embedded kidney tissues were sectioned, and H&E or PAS staining was performed by the Research Histology Core Lab at the University of Virginia. In brief, 5 μm-thick sections were stained with hematoxylin (0.1%) for 5 min and eosin (0.5%) for 1 min. The sections were viewed using a light microscope (Xeiss Axiolmager Z1/Apotome microscope, Carl Zeiss, Oberkochen, Germany). PAS stains carbohydrates on the surface of proximal tubule epithelial cells, which is useful to assess tubular injury.

## Statistical analysis

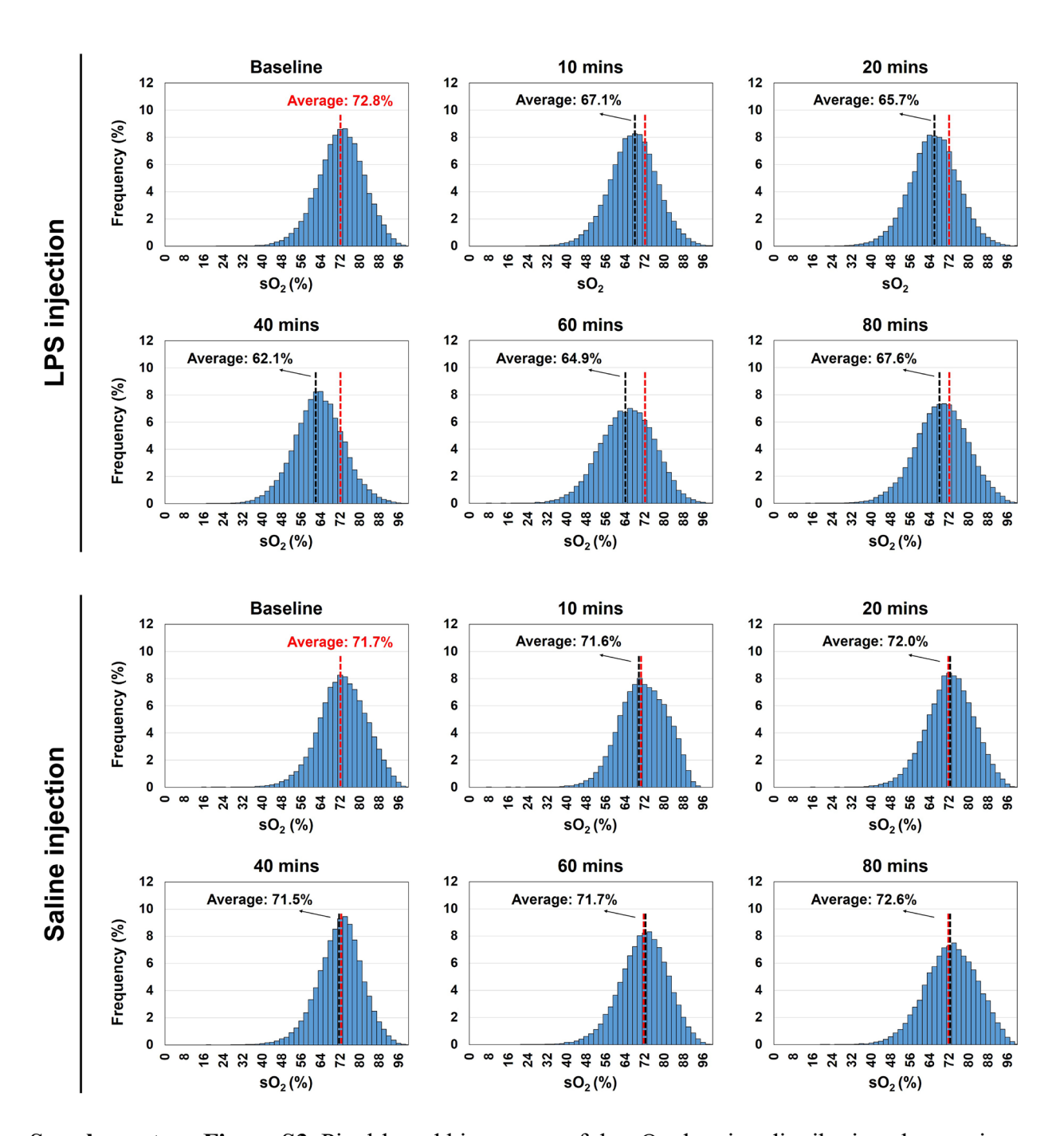
Two-way repeated measures ANOVA was used to compare hemodynamic changes, as well as plasma creatine and ATP changes in the LPS- vs. saline-injected group (Figure 4, Figure 5b–c, and Supplementary Figure S6) with Bonferroni correction. All data were presented in the form of mean  $\pm$  standard error of the mean. In all statistical analyses, p < 0.05 was considered significant.



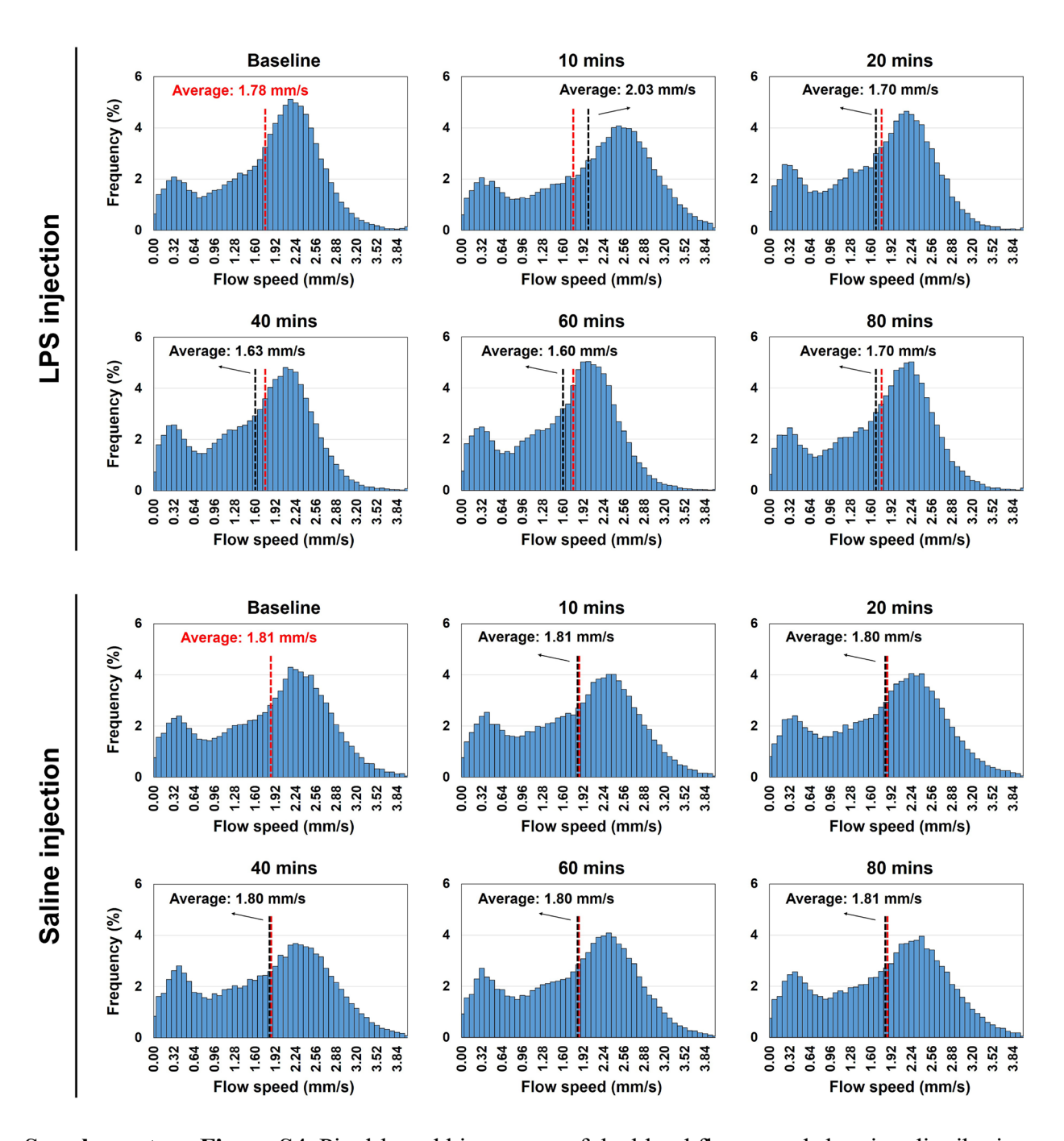
**Supplementary Figure S1.** Photoacoustic microscopy (PAM) system for intravital imaging of mouse kidney. (a) System schematic. BPF, bandpass filter; BS, beam sampler; DBS, dichroic beamsplitter; FC, fiber collimator; NDF, neutral-density filter; PD, photodiode; PM-SMF, polarization-maintaining single-mode fiber; SMF, single-mode fiber. Close-up view: scanning head. DL, doublet; CL, correction lens; UT, ring-shaped ultrasonic transducer. (b) Photograph of the experimental setting, showing a surgically exposed and immobilized mouse kidney in the 3-D printed kidney cup. (c) Imaging area, which is highlighted by the white dashed box (1 mm × 1mm).



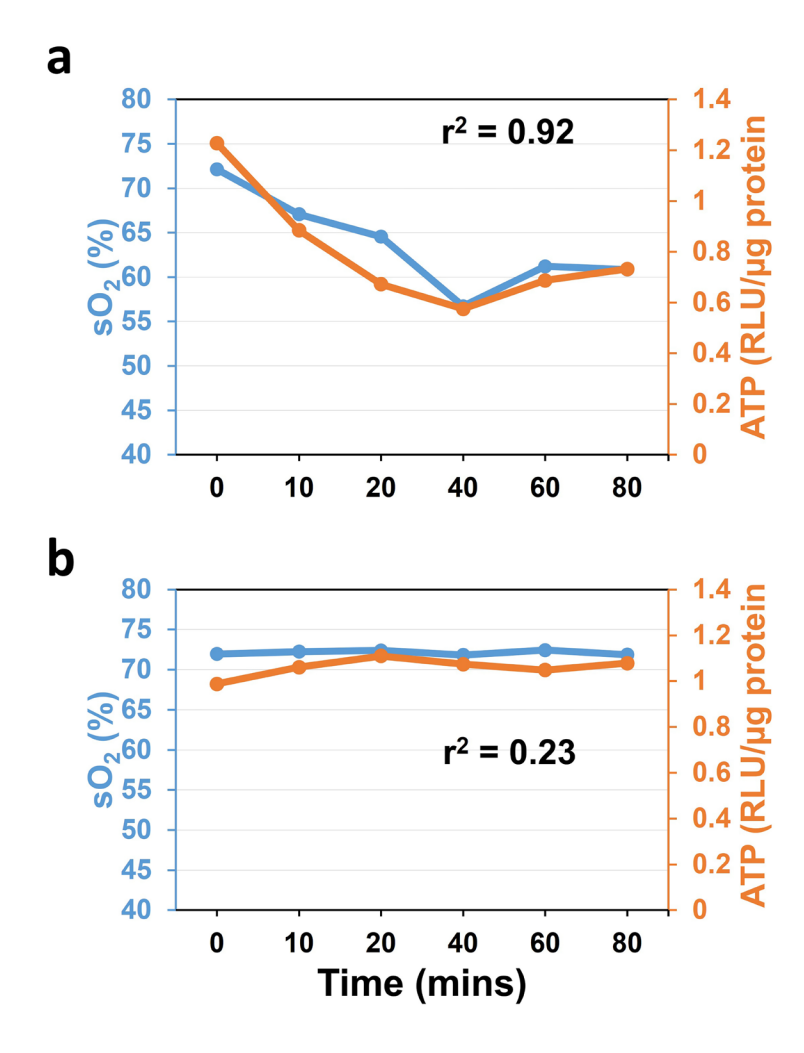
**Supplementary Figure S2.** Time-lapse PAM of microvascular and oxygen-metabolic responses of mouse kidney to saline injection as a control. **(a-d)** C<sub>Hb</sub>, sO<sub>2</sub>, blood flow speed, and MRO<sub>2</sub> images acquired before, 10 minutes, 20 minutes, 40 minutes, 60 minutes, and 80 minutes following LPS, respectively. Scale bar: 200 μm. This experiment was repeated in three animals.



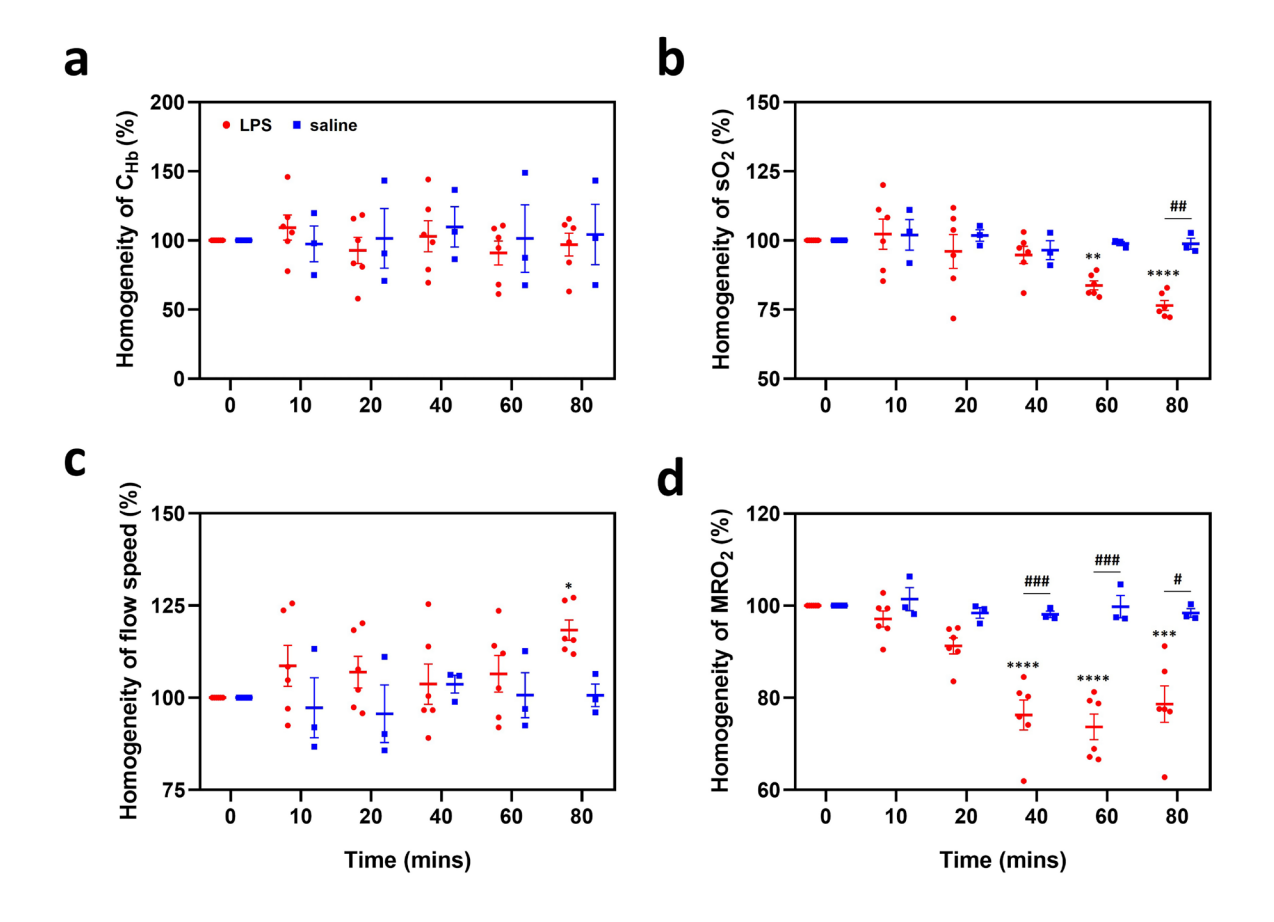
**Supplementary Figure S3.** Pixel-based histograms of the sO<sub>2</sub> showing distribution changes in response to LPS injection, compared to the control (saline injection). Red dashed line: average sO<sub>2</sub> value measured at the baseline (*i.e.*, pre-injection). Black dashed lines: average sO<sub>2</sub> values measured at different time points post-injection (*i.e.*, 10 minutes, 20 minutes, 40 minutes, 60 minutes, and 80 minutes).



**Supplementary Figure S4**. Pixel-based histograms of the blood flow speed showing distribution changes in response to LPS injection, compared to the control (saline injection). Red dashed line: average flow speed measured at the baseline (*i.e.*, pre-injection). Black dashed lines: average flow speeds measured at different time points post-injection (*i.e.*, 10 minutes, 20 minutes, 40 minutes, 60 minutes, and 80 minutes).



Supplementary Figure S5. Regression analysis of the kidney ATP level (RLU/ $\mu$ g protein) and sO<sub>2</sub> (%) for (a) LPS- and (b) saline-injected groups. Data are derived from Figures 4 and 5.



**Supplementary Figure S6.** Heterogeneity analysis of the microvascular and oxygen-metabolic responses of mouse kidney to LPS vs. saline treatment. **(a-d)** C<sub>Hb</sub>, sO<sub>2</sub>, blood flow speed, and MRO<sub>2</sub>, respectively. \*p<0.05, \*\*p<0.01, \*\*\*p<0.001, and \*\*\*\*p<0.0001 indicate statistically significant differences from the corresponding baseline values acquired at 0 min (i.e., before treatment). \*p<0.05, \*\*p<0.01 and \*\*\*\*p<0.001 indicate the statistically significant differences between the time-matched measurements in the LPS- (n = 6) and saline-treated (n = 3) groups. Data are presented as mean ± SEM.

## **Supplementary References**

- S1. Ning B, Kennedy MJ, Dixon AJ, et al. Simultaneous photoacoustic microscopy of microvascular anatomy, oxygen saturation, and blood flow. *Opt Lett.* 2015;40:910-913.
- S2. Ning B, Sun N, Cao R, et al. Ultrasound-aided Multi-parametric Photoacoustic Microscopy of the Mouse Brain. *Sci Rep.* 2015;5:18775.
- S3. Wang T, Sun N, Cao R, et al. Multiparametric photoacoustic microscopy of the mouse brain with 300-kHz A-line rate. *Neurophotonics*. 2016;3:045006.
- S4. Gigliotti JC, Huang L, Ye H, et al. Ultrasound prevents renal ischemia-reperfusion injury by stimulating the splenic cholinergic anti-inflammatory pathway. *J Am Soc Nephrol*. 2013;24:1451-1460.
- S5. Mohanaiah P, Sathyanarayana P, GuruKumar L. Image texture feature extraction using GLCM approach. *IJSRP*. 2013;3:5.
- S6. Inoue T, Abe C, Sung SJ, et al. Vagus nerve stimulation mediates protection from kidney ischemia-reperfusion injury through α7nAChR<sup>+</sup> splenocytes. *J Clin Invest*. 2016;126:1939-1952.
- S7. Keppler A, Gretz N, Schmidt R, et al. Plasma creatinine determination in mice and rats: An enzymatic method compares favorably with a high-performance liquid chromatography assay. *Kidney Int*. 2007;71:74-78.